Journal of Structural Geology 127 (2019) 103868

Contents lists available at ScienceDirect

Journal of Structural Geology

journal homepage: www.elsevier.com/locate/jsg

Microstructurally-constrained versus bulk fault gouge K-Ar dating

Thomas Scheiber[a,b,*], Giulio Viola[c], Roelant van der Lelij[b], Annina Margreth[b], Jasmin Schönenberger[b]

[a] Western Norway University of Applied Sciences, Sogndal, Norway
[b] Geological Survey of Norway, Trondheim, Norway
[c] Department of Biological, Geological and Environmental Sciences, University of Bologna, Italy

ARTICLE INFO

Keywords:
Brittle deformation
Fault rock
K–Ar dating
Pseudotachylyte
Microstructure
SW Norway

ABSTRACT

Structural, mineralogical and geochronological data were collected from two brittle fault zones (Fault I and II) deforming the Ordovician Rolvsnes granodiorite in SW Norway. Microstructurally-constrained K–Ar data from cohesive damage zone samples are compared to bulk K–Ar data from fault gouges from the adjacent fault cores. In Fault I, fluid ingress along the fault core caused pervasive alteration of the host granodiorite. Plagioclase and biotite are almost completely altered to kaolinite, quartz, illite and smectite. In Fault II, a complex deformation history is recorded by multiple fault rock microdomains, including an ultracataclasite with > 50% authigenic illite and an illite/jarosite-bearing pseudotachylyte. Microdomains hosting authigenic illite (± jarosite) from both studied faults were separated, characterized mineralogically and dated by K–Ar. Results confirm that each domain contains only one generation of authigenic illite (± jarosite), and provide robust time constraints on fault initiation in the Carboniferous (339 ± 8 Ma) and reactivation in the Permian (289 ± 6 Ma). K–Ar geochronology of the adjacent fault gouges yields inclined age-versus-grain-size relationships. The ages of the coarsest grain size fractions are similar to the age range of the damage zone data, whereas the ages of the finer fractions are significantly younger. Our study provides new and important insights into the dynamics of long-lived fault zones: Isotopic signatures and structural features representative of fault initiation are preserved in the damage zones, while they are progressively overprinted due to cumulative strain localization in the fault cores. Finally, our study further clarifies the significance of 'age plateaus' in age-versus-grain-size plots, which allows for a robust and geologically meaningful interpretation of K–Ar data.

1. Introduction

Brittle fault zones are the expression of localized slip in response to the accommodation of tectonic stresses in the lithosphere. Such fault zones are generally composed of a fault core, which accommodates most of the displacement and hosts brittle fault rocks, and an associated damage zone, where the density of brittle deformation features decreases away from the fault core (Caine et al., 1996). The pressure-sensitive dilational nature of brittle deformation commonly causes influx of fluids in the deforming rock, which allows for the enhanced mobilization of elements during faulting (e.g., Marchesini et al., 2019). The chemical composition of the involved fluid phase, together with other physical factors such as temperature, frictional properties, stresses and strain rate, determine the type of brittle fault rock that forms during deformation (Sibson, 1977; Snoke et al., 2014). Cataclasite, fault gouge and fault breccia form by a combination of processes leading to mechanical comminution of the faulted host rock and neocrystallization of authigenic mineral phases, whereas pseudotachylyte forms from the generation of frictional melt and is thus commonly regarded as indicative of slip at seismic velocities (e.g., Cowan, 1999; Lin, 2008).

Studies aiming at constraining the age of movement in brittle fault zones generally concentrate on fault rocks from the fault core, where the K-bearing phyllosilicate illite, which is amenable to K–Ar dating (e.g., Clauer, 2013; Tagami, 2012), may form as a syn-kinematic authigenic mineral phase (Haines and van der Pluijm, 2012; Vrolijk and van der Pluijm, 1999). Illite can form by illitization of fragmented smectite (Altaner and Ylagan, 1997), by breakdown of K-feldspar (Zwingmann et al., 2010), by hydration reactions of mica or by neocrystallization from a fluid phase (Mancktelow et al., 2015). Illite geochronology is usually performed on multiple grain size fractions of the same fault rock sample and K–Ar data are commonly reported as age-versus-grain-size plots (Pevear, 1999), commonly referred to as K–Ar age spectra (Torgersen et al., 2015). K–Ar data from fault rocks,

* Corresponding author. Røyrgata 6, 6856, Sogndal, Norway.
E-mail address: thomas.scheiber@hvl.no (T. Scheiber).

https://doi.org/10.1016/j.jsg.2019.103868
Received 19 October 2018; Received in revised form 27 June 2019; Accepted 21 July 2019
Available online 02 August 2019

however, may at times be difficult to interpret, mainly because of the following two aspects: (1) The dated grain size fractions may contain other K-bearing phases in addition to a single generation of authigenic illite (Zwingmann and Mancktelow, 2004). Additional non-synkinematic K-bearing phases can be derived from protolithic components or from older illite generations, leading to older K–Ar ages (Solum et al., 2005); occasionally, K-bearing phases may be represented by authigenic minerals other than illite. (2) The actual process responsible for authigenesis often remains unclear. Illite may grow during slip localization, but pre- or post-deformational hydrothermal alteration (Viola et al., 2013), diagenesis (Lanson et al., 2002) or deep weathering (Fredin et al., 2017) may also contribute to the crystallization of K-bearing phases. In addition, thermally activated volume diffusion can lead to partial or complete resetting of the initial K–Ar ages (Torgersen et al., 2014).

If a fault rock solely contains one generation of authigenic illite, the age-versus-grain-size spectrum derived from the dating of multiple grain size fractions is a flat 'age plateau' whereby the ages of all dated grain size fractions are identical and the dated authigenic K-bearing mineral phases formed during one single phase of deformation. Age plateaus in K–Ar grain-size spectra are, however, rarely obtained, especially when dealing with faults in geologically old basement terranes, which are prone to multiple episodes of deformation (e.g., Davids et al., 2013; Koehl et al., 2018; Torgersen et al., 2014). Fault reactivation as a result of varying stress boundary conditions, together with the possibility that fault zones potentially act as a conduit for fluids (Bense et al., 2013; Caine et al., 1996; Rutter et al., 2001), may indeed affect the K–Ar radiogenic system of the fault rock forming minerals (Verdel et al., 2012), and inclined K–Ar age spectra become thus the typical outcome of K–Ar fault rock geochronology, with K–Ar ages increasing with grain size (e.g., Torgersen et al., 2015). The detailed mineralogical characterization of each dated grain size fraction by X-ray diffraction (XRD), illite polytype determination (e.g., Ylagan et al., 2002) and transmission electron microscopy (TEM), are commonly used to decipher the different origins and generations of the K-bearing minerals. Additionally, a detailed multiscalar structural characterization of the fault zone architecture (Viola et al., 2016), stable isotope studies (Mancktelow et al., 2015) and the determination of illite crystallinity (Verdel et al., 2011) may help to constrain the influence of specific processes on the authigenesis of illite.

All the aspects above, however, may be effectively tackled, and a solid background to a reliable interpretation of K–Ar fault rock data provided, if K–Ar geochronology is performed on K-bearing phases that are extracted from well-constrained microstructural domains containing clear textural relationships between the authigenic and the pre-faulting phases (cf. Viola et al., 2016). In addition, the smaller the microstructural domain analyzed and dated, the greater the chance to separate and date only one generation of authigenic K-bearing minerals.

Here, we present a case study from two fault zones located in SW Norway (Bømlo archipelago), which highlights the usefulness of linking microstructural investigations of fault rock with spatially-controlled dating of carefully separated authigenic mineral phases to improve the understanding of K–Ar fault rock data and the reliability of their interpretation. Our study of the two faults demonstrates that K–Ar age plateaus, constraining only the earliest increments of fault evolution, are preserved in cohesive rock specimens from the fault damage zones, whereas incohesive fault rocks from the fault cores contain age components tracking the entire fault history, from initiation to reactivation, and the effects of rock interaction with infiltrating reactive fluids. Our study area lies within a recently investigated c. 50 km^2 area with a high spatial density of illite K–Ar ages (this study; Fredin et al., 2017; Scheiber and Viola, 2018; Viola et al., 2016). Such a K–Ar date density allows for a thorough comparison between the new data presented here and the existing regional K–Ar dataset from Bømlo, which may serve as a baseline for improving future interpretations of fault rock K–Ar data in general.

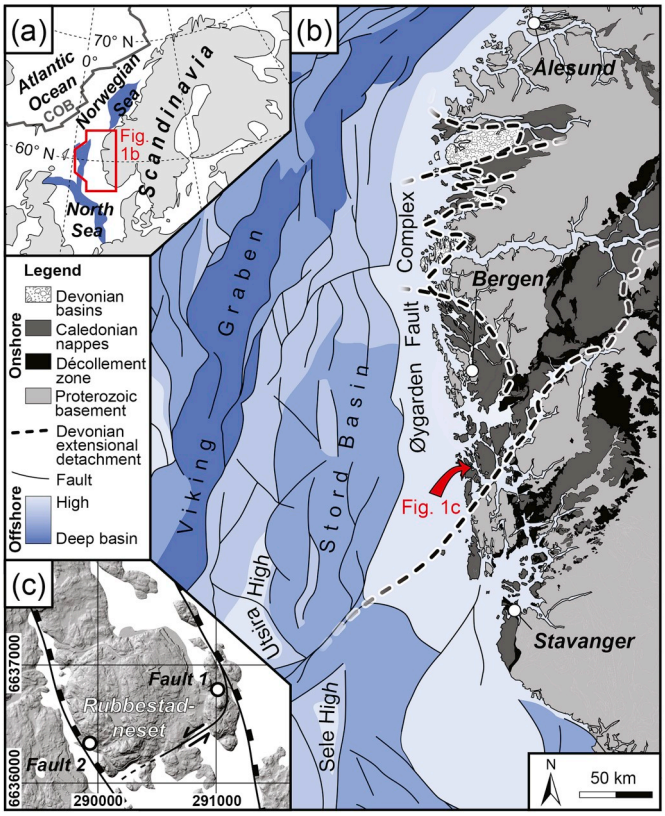

Fig. 1. (a) Map of the eastern North Atlantic realm. Major rift elements of the North Sea and the Norwegian Sea are shown in blue. COB = continent-ocean boundary. (b) Simplified tectonic map of SW Norway and the northern North Sea. (c) Hill-shaded digital elevation model of the Rubbestadneset peninsula (Bømlo archipelago). Location of studied faults and traces of major faults are indicated. (For interpretation of the references to color in this figure legend, the reader is referred to the Web version of this article.)

2. Geological framework

The studied faults are located in coastal SW Norway (Fig. 1) and deform the Mid-Ordovician (c. 466 Ma) Rolvsnes granodiorite (Andersen and Jansen, 1987; Scheiber et al., 2016). The Rolvsnes granodiorite is interpreted as belonging to an accreted arc system, which became part of the Caledonian orogenic prism as a coherent nappe translated southeastward onto Proterozoic basement (Fig. 1b) during the Silurian-Devonian Caledonian orogeny (Corfu et al., 2014; Stephens and Gee, 1989). Subsequent late-Caledonian Devonian extension accommodated by large, ductile hinterland-directed shear zones significantly thinned the orogenic wedge (Fossen, 2010).

By the Mid-Late Ordovician (c. 460 Ma), the granodiorite had cooled to below 300–400 °C and, since then, resided at high structural levels (Scheiber et al., 2016), which resulted in a complex record of brittle deformation features accumulated mainly during Caledonian tectonics and later multiple episodes of crustal extension during the North Sea rift evolution (Fig. 1b). K–Ar data from faults dissecting the Rolvsnes granodiorite constrain faulting in the Permo-Triassic, Late Triassic-Late Jurassic and Early Cretaceous (Scheiber and Viola, 2018; Viola et al., 2016). The former two episodes are associated with enhanced exhumation of the greater coastal realm of SW Norway, as constrained by apatite fission-track thermochronology (Fossen et al., 2017; Ksienzyk et al., 2014). According to low-T thermal modelling (op. cit.), the basement units reached surface conditions at ca. 160 Ma and were subsequently reburied. For a detailed description of the regional geological and structural framework and of the spatial and temporal evolution of the fracture pattern preserved in the area, the reader is

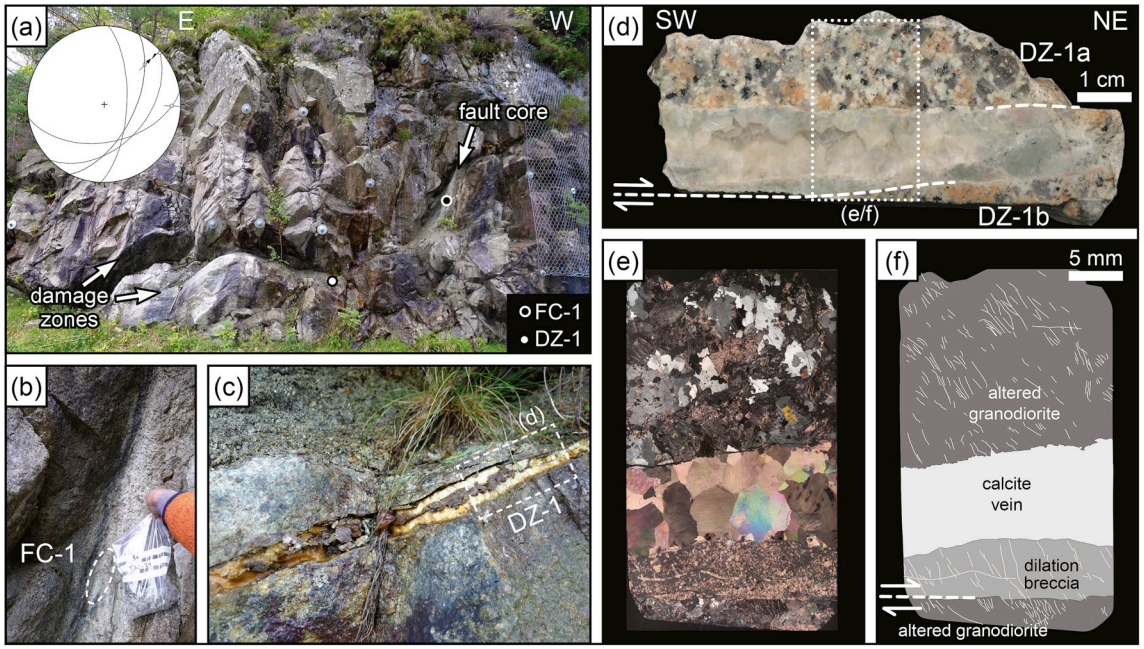

Fig. 2. (a) Fault I. A curved fault plane is associated with top-to-the-NE strike slip kinematics, (b) an up to 25 cm thick band of fault gouge in the fault core and (c) fault-plane parallel calcite veins in the damage zone. (d) Scan of sample DZ-1. Dotted rectangle indicates location of area covered by the (e) cross-polarized light micrograph and (f) interpretation of the thin section. Bright lines correspond to calcite micro-veins indicating overall dextral shear (translating to top-to-the-NE).

referred to Scheiber and Viola (2018).

3. Fault and sample description

The two studied fault zones outcrop in well-exposed road sections located along the eastern and western coastline of the Rubbestadneset peninsula (Fig. 1c), Bømlo archipelago (SW Norway). Both faults relate to larger c. NNW-SSE-striking fault zones whose cores remain largely in the fjords (Fig. 1c).

3.1. Fault I (samples FC-1, DZ-1)

Fault I is characterized by a gently curved fault plane, which changes orientation from steeply E-dipping in the west to steeply SSE-dipping in the east and is associated with strike-slip lineations (Fig. 2a). The fault core contains an up to 25 cm thick fault gouge (Fig. 2b), and calcite veins cut the surrounding damage zone (Fig. 2c). Sample FC-1 is from the fault gouge (Fig. 2b), whereas sample DZ-1 is from the immediate footwall damage zone (Fig. 2c). DZ-1 is characterized by a c. 2 cm thick fault plane-parallel calcite vein (Fig. 2d–f), which is sandwiched between the overlying altered host granodiorite grading into the incohesive gouge of the fault core (DZ-1a), and an underlying breccia and another domain of altered granodiorite (DZ-1b). Striations at the base of the breccia and the orientation of tensile fractures filled with calcite indicate dextral shear, i.e. top-to-the-NE (Fig. 2f). The magmatic texture is still well-preserved in the altered granodiorite (cf. Fig. 2d), although scanning electron microscope (SEM) imaging shows that the mineralogy of this rock has changed significantly since its crystallization (Fig. 3). Alteration products are mainly kaolinite, quartz, illite/smectite aggregates and individual illite crystals up to 30 µm long (Fig. 3a and b). Veins, filled with calcite and minor kaolinite, commonly crosscut protolithic quartz and K-feldspar, while plagioclase is completely replaced by alteration products (Fig. 3c and d). Similarly, biotite is heavily altered and largely replaced by kaolinite, quartz and illite/smectite (Fig. 3e). The breccia of sample DZ-1 (Fig. 2e and f) is characterized by calcite clasts speckling a fine-grained matrix composed of kaolinite and quartz (Fig. 3f). No K-bearing phases were detected in the breccia. In sample DZ-1, illite is thus clearly the result of fluid-induced alteration.

3.2. Fault II (samples FC-2, DZ-2)

Fault II is a moderately NE-dipping normal fault whose core hosts an up to 60 cm thick, dark-green to black lens of clay-rich fault gouge (Fig. 4a and b). Discrete slip surfaces wrap around the lens. Striations plunge towards the northeast and calcite veins and Riedel shears invariably indicate a top-to-the-NE, i.e. normal, sense of movement. Sample FC-2 is from the gouge (Fig. 4b), and sample DZ-2 is a cohesive slab from right above a distinct slip surface in the immediate upper damage zone (Fig. 4c).

Under the microscope, seven different fault rock domains and seven different types of calcite mineralizations could be recognized and mapped (Fig. 4d–f). Crosscutting relationships indicate that fault rock domains 1 and 2 are the oldest and domain 7 is the youngest. Domain 1 contains clasts of domain 2 and vice versa (cf. Fig. 4f) and domains 2 to 4 occur together as a layered boudin, which may indicate that fault rock domains 1–4 formed contemporaneously. The relative chronology among the different calcite mineralizations is less clear, but the blocky impure calcite mineralization (I in Fig. 4f) seems to be the oldest, while the pure blocky calcite veins and the elongate to blocky calcite grown in syntaxial veins (VI and VII in Fig. 4f) are interpreted as the youngest and as directly related to deformation along the discrete slip surfaces associated with fault rock domain 7.

The modal composition of each fault rock domain (Fig. 5) was quantified on the basis of the different mineral grayscales in SEM-BSE (backscattered electrons) images using the threshold tool of the ImageJ software (Schneider et al., 2012). Illite occurs in fault rock domain 1 (~60%) and domain 7 (~4%). Domain 1 corresponds to an ultracataclasite, in which illite forms a dense network of platy crystals (Figs. 5b and 6a) with a relatively large average grain size of ~4 µm (Fig. 6b). Secondary quartz, kaolinite and accessory minerals (including the K-bearing Fe-sulfide jarosite) speckle the illite mass. Microstructural relationships indicate that all the minerals composing domain 1 formed cogenetically during one faulting event. Fault rock domain 7 is associated with discrete slip surfaces and contains a pseudotachylyte vein (Fig. 4d–f, 6c-f). Its lower margin is cryptocrystalline to glassy whereas

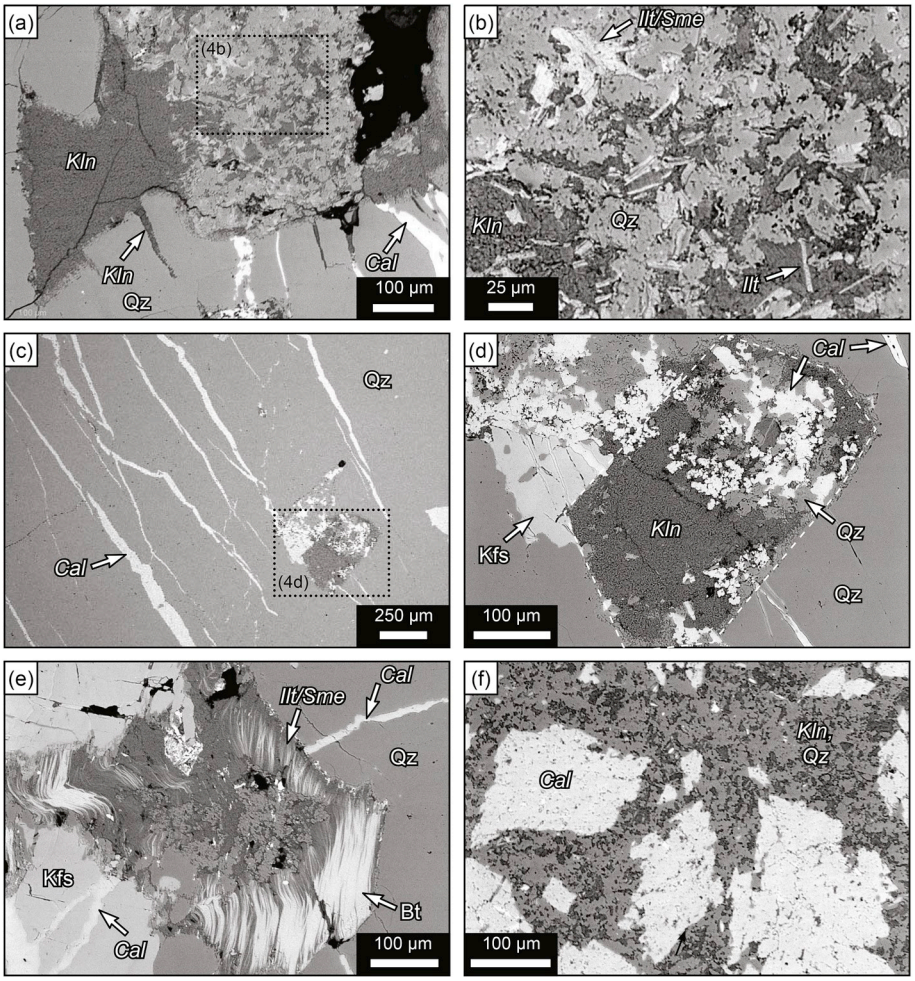

Fig. 3. SEM-BSE (backscattered electrons) images of the altered granodiorite of sample DZ-1 (cf. Fig. 2d–f). (a) Fractures in protolithic quartz grain are filled by calcite and kaolinite. (b) Completely altered zone containing secondary quartz, kaolinite, illite-smectite aggregates and illite single crystals up to 30 µm in size. (c) Protolithic quartz grain crosscut by calcite veins and hosting an (d) altered inclusion mainly composed of kaolinite, quartz and calcite. Stippled outline indicates the idiomorphic shape of a "ghost plagioclase". (e) "Ghost biotite". The major substitutes are kaolinite, quartz and illite/smectite mixed layers (f) Microstructure of the breccia (cf. Fig. 2e and f). characterized by kaolinite-quartz groundmass speckled by angular and poorly sorted calcite clasts. Primary (protolithic) minerals are given in regular font, secondary (authigenic) minerals are given in italic font.

the pseudotachylyte vein becomes progressively richer in quartz, illite and kaolinite moving upward (Fig. 6e and f). Newly-grown Fe-sulfide (jarosite) and Fe-oxide (hematite) crystals are dispersed in this domain, which is indeed a common feature in pseudotachylytes (Kirkpatrick and Rowe, 2013). Illite of domain 7 occurs as up to 35 µm long individual single crystals (Fig. 5h), and is thus different from the illite mesh of domain 1 (Fig. 5b). In summary, sample DZ-2 contains two generations of faulting-related illite (and jarosite) that are spatially confined to fault rock domain 1 and fault rock domain 7.

4. Mineralogical characterization and K–Ar geochronology

4.1. Analytical methods

All samples were characterized by X-ray diffraction (XRD) mineralogical quantification and dated by K–Ar at the NGU (Geological Survey of Norway), except FC-2 which was analyzed at CSIRO (Commonwealth Scientific and Industrial Research Organization, Australia). The detailed description of the analytical approach used at the NGU and the analytical details of the CSIRO laboratory are provided as supporting material to this paper (Supplement material 1). XRD data were used to determine illite crystallinity expressed by the Kübler Index (Kübler and Jaboyedoff, 2000) and standardized according to Warr (2018). There was too little sample material to perform XRD analysis of the < 0.1 µm fraction of sample FC-1. Together with the < 0.1 µm fraction of FC-2, it was therefore, investigated by TEM (transmission electron microscopy) for further mineralogical characterization (Supplement material 1). TEM enables detection, imaging and analysis of K-bearing phases below the detection limit of XRD analysis (1–2 wt%).

4.2. Results

A total of six samples were chosen for K–Ar geochronology (Table 1, Fig. 7). These samples correspond to (1) fault gouge (FC-1, Fig. 2b), (2) altered granodiorite from above the calcite vein (DZ-1a, Fig. 2d), (3) breccia and altered granodiorite from below the calcite vein (DZ-1b, Fig. 2d) from Fault I (Fig. 7a), and (4) fault gouge (FC-2, Fig. 4b), (5) fault rock domain 1 (DZ-2a, Fig. 4d), (6) fault rock domain 7 (DZ-2b, Fig. 4d) from Fault II (Fig. 7b). The two illite-bearing fault rock domains of sample DZ-2 were physically separated using a micro-saw.

The two gouge samples from the fault cores yielded five grain size fractions (< 0.1, 0.1–0.4, 0.4–2, 2–6, 6–10 µm; except the largest fraction of FC-2), while the four samples from the damage zones contained enough material only for the three coarsest grain size fractions (Table 1). The lack of the two smallest grain size fractions in the damage zone samples is in accordance with the average coarse grain size observed in these samples during SEM imaging (Figs. 3, 5 and 6).

4.2.1. Mineralogy of the dated grain size fractions

XRD analysis of each dated fraction (except the < 0.1 µm fraction of FC-1) shows that illite is the dominant K-bearing phase in all samples (Fig. 8, Supplement material 2 and 3). Additional K-phases are jarosite, which occurs in all grain size fractions of DZ-2a and DZ-2b, and K-feldspar which was detected only in small amounts in the coarsest grain size fraction of DZ-1b and the two coarsest fractions of FC-2. No K-bearing mineral phase was detected by XRD in the two smallest grain size fractions of FC-1 (Fig. 8a). However, their K contents range between 0.11% and 1.13% (Table 1) and TEM analysis of the < 0.1 µm fraction of FC-1 indicate that K occurs in smectite-illite mixed layers

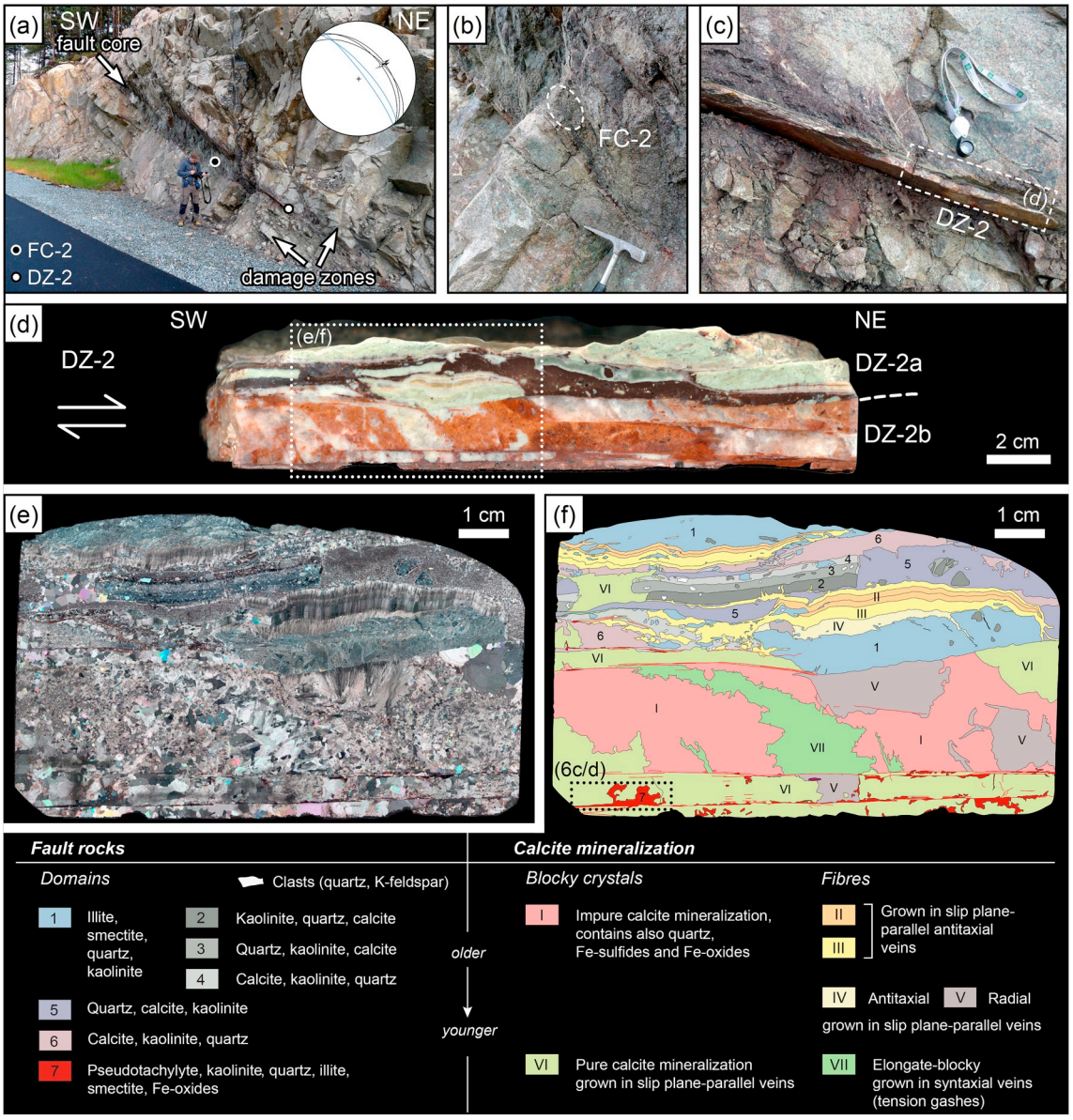

Fig. 4. (a) Outcrop photograph of the top-to-the-NE normal Fault II. (b) Fault gouge sampling location. (c) Striated calcite surface separating highly-fractured footwall rock from cohesive fault rock and damage zone in the hanging wall. (d) Scanned surface of DZ-2. Dotted rectangle indicates the location of the thin section shown as cross-polarized micrograph in (e). (f) Interpretation of the thin section based on cross-polarized, plane-polarized microscopy and SEM analysis. Seven fault rock domains and seven different types of calcite mineralization were identified. Red lines indicate discrete slip planes that are associated with the pseudotachylyte-hosting fault rock domain 7. Dominant mineral content for each domain is given (for detailed mineralogy of each domain, see Fig. 5). Clasts smaller than ~100 µm are not shown. (For interpretation of the references to color in this figure legend, the reader is referred to the Web version of this article.)

(Fig. 8c). Illite crystallinity values (Kübler indices) are generally low (0.17–0.33) for the DZ-1 samples and range between 0.32 and 0.46 for DZ-2 samples (Supplement material 3).

4.2.2. K–Ar results

K–Ar ages from the damage zone of Fault I (DZ-1a/b, Figs. 2c and 7a) range between 340 ± 7 Ma and 282 ± 7 Ma (Fig. 9a, Table 1). Data from the adjacent gouge sample (FC-1, Figs. 2b and 7a) define an inclined age spectrum, where the age of the coarsest grain size fraction is the oldest (335 ± 8 Ma) and is identical to the ages of the coarsest grain size fractions of DZ-1a and DZ-1b (Fig. 9a). A weighted mean calculation of these three oldest ages from Fault I yields 339 ± 8 Ma (MSWD = 0.1). The age of the finest grain size fraction of FC-1 (87 ± 5 Ma) is the youngest in the dataset.

All six K–Ar ages constraining cogenetic growth of illite and jarosite in the two micro-domains of site II (DZ-2a/b, Figs. 4f, 6b and 6f) are identical within error and thus define a plateau (Fig. 9b, Table 1). A weighted mean age of 289 ± 5 Ma (MSWD = 0.7) was calculated for this plateau. The K–Ar data from the adjacent fault gouge (FC-1, Fig. 4b) define an inclined age spectrum with the age of the coarsest (2–6 µm) fraction (273 ± 6 Ma) being slightly younger than the c. 289 Ma age plateau, and an age of 176 ± 4 Ma for the finest grain size fraction (Fig. 9b).

5. Interpretation and discussion

5.1. What do damage zones preserve?

The microstructurally-constrained dating of cohesive rock specimens from the damage zones yields a generally small spread in K–Ar ages for each sample compared to the large age spreads obtained from the adjacent fault core gouges (Fig. 9a and b). The two K–Ar datasets

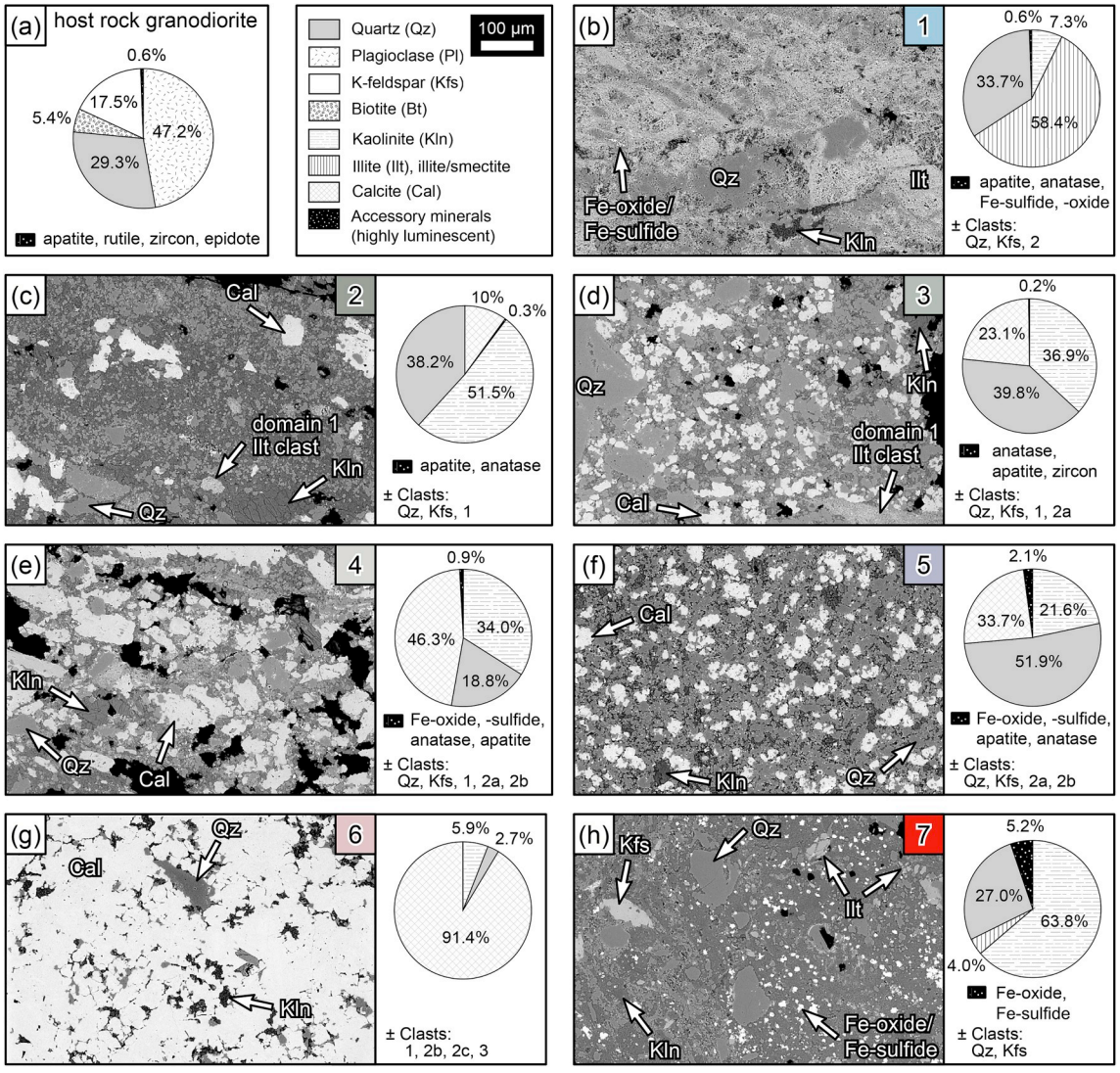

Fig. 5. (a) Modal composition of the fresh Rolvsnes granodiorite (data from Andersen and Jansen, 1987) versus (b-h) mineralogy of each fault rock domain identified in sample DZ-2. A representative SEM image for each domain is provided. Note that plagioclase and biotite make up together > 50% of the fresh granodiorite, but do not occur in the fault rocks. Kaolinite, illite, illite-smectite mixed layers, calcite and Fe-oxides are the authigenic and synkinematic phases. Clasts are represented by protolithic quartz, K-feldspar or older fault rock lithons. Fault rock domain 1 (b) contains > 50% illite, and fault rock domain 7 (h) contains a pseudotachylyte injection close to the slip surface (cf. Fig. 6). Modal analysis was carried out for the fault rock structurally above the pseudotachylyte. It is characterized by the highest kaolinite (c. 64%) and Fe-oxide/Fe-sulfide (c. 5%) content and by occurrence of illite (4%).

from the damage zone of Fault I (DZ-1a/b) yield a narrow age range of c. 340-320 Ma (Table 1, Fig. 9a), whereas the age of the finest fraction of DZ-1a is significantly younger (282 ± 7 Ma). As for sample DZ-2, the ages of all the dated grain size fractions are identical within error (Fig. 9b) and thus define a K–Ar age-versus-grain-size plateau. Such plateaus, ideally defined by all dated grain size fractions of a single sample/microdomain, can be interpreted as indicative of pervasive authigenesis of K-bearing minerals during a specific period of deformation and/or fluid flow and thus allow, in contrast to the much more commonly-obtained inclined age spectra (e.g., Pevear, 1999; Torgersen et al., 2015), a direct correlation of age data and specific structural features.

The weighted mean age from Fault I (339 ± 10 Ma, Fig. 9a) may constrain a significant phase of authigenic illite growth. Traces of protolithic K-feldspar were, however, identified by XRD in the coarsest fraction of DZ-1b (Fig. 8a) and SEM images from DZ-1 show indeed remnants of generally coarser (> 10 µm) protolithic K-feldspar (Fig. 3d and e), making the age of c. 340 Ma a maximum age for illite authigenesis. With the exception of this K-feldspar occurrence in DZ-1b, mineralogical characterization does not help to explain the c. 340-320 Ma age spread of DZ-1b and the inclined age spectrum of DZ1-a (Fig. 9a). Illite crystallinity values for DZ-1 samples are generally low and correlate to temperatures of c. 300 °C (Fig. 10, Supplement material 3). At temperatures of c. 300 °C, thermally activated volume diffusion of radiogenic ^{40}Ar can cause complete resetting of the initial K–Ar age of grain sizes < 2 µm, whereas the age of 10 µm grains is fully reset only above temperatures of c. 350 °C (Torgersen et al., 2014). Therefore, the Carboniferous age of 339 ± 8 derived from the three coarsest (6–10 µm) grain size fractions (Fig. 9a) can be regarded as the best approximation for illite authigenesis in DZ-1 whereas the younger ages of the finer grain size fractions of DZ-1 are the result of thermally activated volume diffusion. The illite-forming process can be tentatively related to hydration of K-feldspar and biotite (Haines and van der Pluijm, 2012; Zwingmann et al., 2010) during an episode of pervasive fluid-induced alteration as suggested by the preserved magmatic texture and the undeformed character of the sampled rock specimens (Figs. 2d–f, 3a-e). Fluid flow was, however, facilitated and enhanced by NE-SW extension, as indicated by suitably-oriented calcite veins and

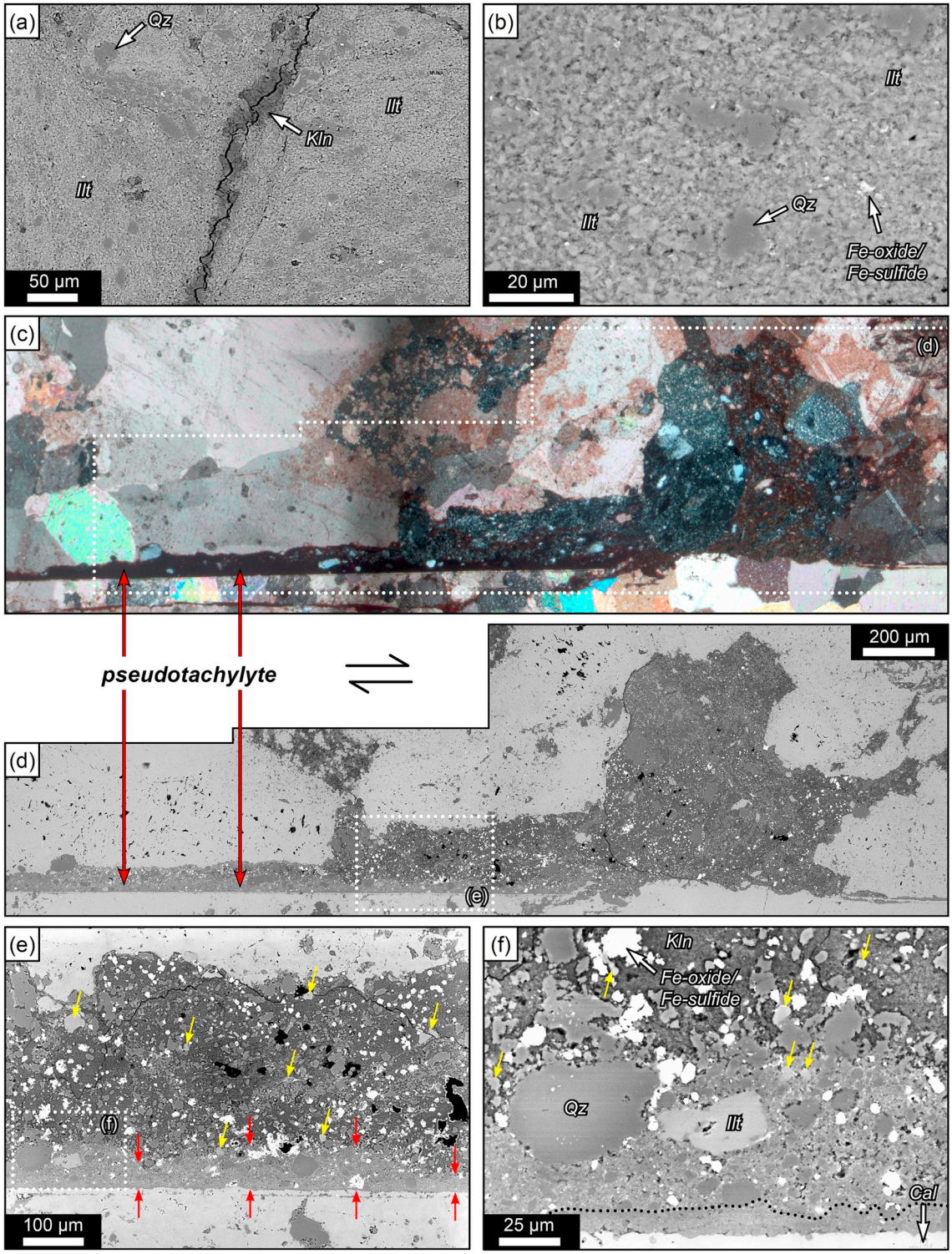

Fig. 6. Images of fault rock domain 1 (a-b) and fault rock domain 7 (c-f) of sample DZ-2 (cf. Fig. 4f). (a) SEM-BSE images of kaolinite-filled vein cutting across the ultracataclasite of domain 1. (b) Mesh of illite speckled by darker quartz grains. (c) Cross-polarized micrographs and (d) SEM images of fault rock domain 7 (sample DZ-2, cf. Fig. 4f). Pseudotachylyte occurs immediately above the main slip surface. (e) The pseudotachylyte is overlain by a darker, kaolinite-rich domain. (f) The pseudotachylyte can be divided into a purely amorphous layer at the base and a clast-bearing layer atop. The stippled black line marks the approximate border between these layers. Clasts are subangular to rounded. Red arrows indicate pseudotachylyte, yellow arrows indicate illite. (For interpretation of the references to color in this figure legend, the reader is referred to the Web version of this article.)

slip-related dilation breccia (Figs. 2c–f, 3f).

The numerous fault rock domains identified in sample DZ-2 (Figs. 4f and 5) also formed during NE-SW extension (as shown by the kinematic analysis of the fault), but they are clearly related to extremely localized and likely short-lived slip episodes, are associated with lower temperatures of c. 200 °C (Fig. 10) and are significantly younger (289 ± 5 Ma). Both microstructurally-constrained samples from DZ-2 yield identical ages for all grain size fractions (Fig. 9b). On the one

Table 1
K–Ar data.

Fault	Sample locality (UTM-32N)		Sample ID	Original Sample ID	Grain size fraction (μm)	^{40}Ar* (mol/g)	^{40}Ar* (%)	K (%)	Age (Ma)	± σ (Ma)
	Easting	Northing								
I	291005	6636800	*FC-1*	*TSC-24*	< 0.1	2.0360E-11	2.8	0.131	87.2	4.7
					0.1–0.4	3.0521E-11	3.7	0.107	158.0	6.7
					0.4–2	6.6810E-11	9.2	0.171	211.9	6.6
					2–6	1.8058E-10	29.7	0.320	299.5	7.8
					6–10	3.3550E-10	40.8	0.525	335.3	8.0
			DZ-1a	*TSC-56a*	0.4–2	2.6448E-10	52.7	0.500	281.8	7.2
					2–6	4.5556E-10	64.7	0.736	325.7	12.4
					6–10	7.7537E-10	73.5	1.195	340.0	7.4
			DZ-1b	*TSC-56b*	0.4–2	3.1359E-10	69.8	0.519	318.6	7.9
					2–6	4.7225E-10	76.6	0.774	321.3	7.3
					6–10	7.4304E-10	82.3	1.145	340.0	7.1
II	289970	6636355	*FC-2*	*TSC-6*	< 0.1	3.5197E-10	49.0	1.100	175.6	3.9
					0.1–0.4	5.9580E-10	70.3	1.310	244.8	5.2
					0.4–2	7.2278E-10	79.1	1.440	268.4	5.8
					2–6	7.3220E-10	82.0	1.430	273.4	5.8
			DZ-2a	*TSC-7a*	0.4–2	1.6006E-09	88.8	3.003	283.8	5.1
					2–6	1.3006E-09	81.3	2.423	285.7	5.4
					6–10	1.2113E-09	81.5	2.187	294.1	5.6
			DZ-2a	*TSC-7b*	0.4–2	3.1329E-10	74.6	0.576	289.2	7.2
					2–6	1.8277E-10	61.0	0.326	297.4	8.1
					6–10	1.4300E-10	52.7	0.267	285.1	7.9

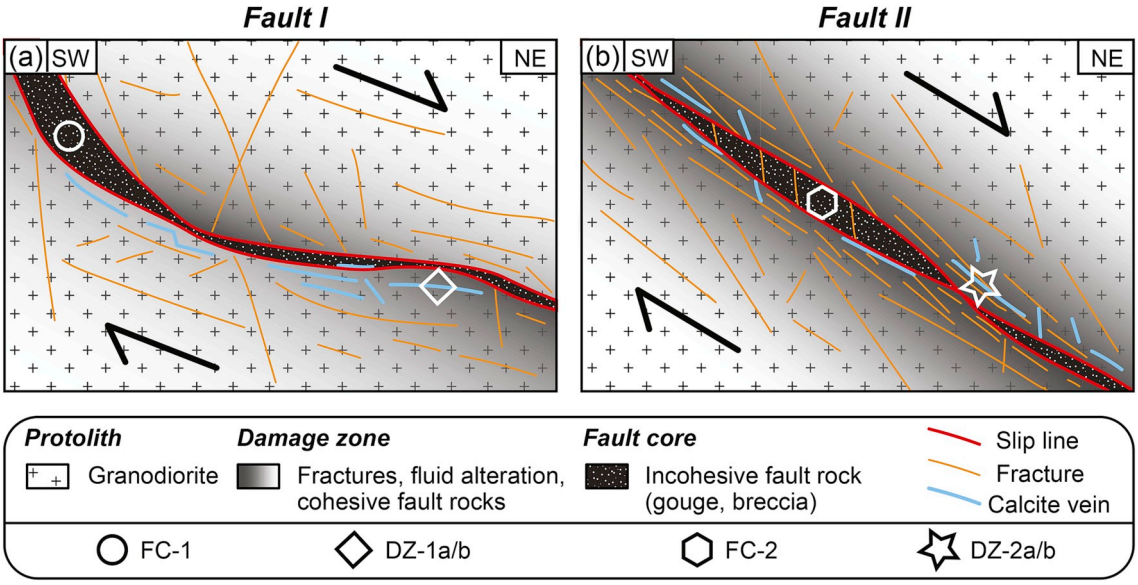

Fig. 7. Schematic illustrations summarizing the structural elements of the investigated fault zones. Sampling locations are shown. Figure not to scale.

hand, the age plateau they define provides a robust time constraint on the growth authigenic illite (and jarosite) during faulting and probably associated seismogenic slip in the Early Permian (289 ± 5 Ma). On the other hand, this result implies that the complex relative age relationships observed at the micro-scale (Fig. 4f) cannot be resolved by the K–Ar method.

The youngest age obtained from DZ-1a (282 ± 7 Ma, Fig. 9a) is identical to the Permian age plateau defined by all ages from DZ-2 (289 ± 5 Ma, Fig. 9b). Sample DZ-1a continuously grades into incohesive fault rock of the fault core (Fig. 2c and d), which opens up the possibility that later (post c. 339 Ma) faulting and/or fluid flow activity in the fault core affected the isotopic system in DZ-1a in addition to thermally activated volume diffusion in the Carboniferous. The presence of illite-smectite mixed layers in DZ-1a (Fig. 3) may indicate that illite formed as a secondary product by illitization of smectite (Altaner and Ylagan, 1997; Haines and van der Pluijm, 2012). However, the illite crystallinity value of the 0.4–2 μm fraction of DZ-1a correlates well with the c. 300 °C temperature regime obtained from the Carboniferous illites from DZ-1 (Fig. 10). Permian fault reactivation may have resulted in recrystallization of the 0.4–2 μm grain size in DZ-1a without changing the original mean consecutive illite layers (i.e. the illite crystallinity), or, alternatively, the youngest age from DZ-1a is a mixed age resulting from Carboniferous and younger illites. The ages from the lower altered granodiorite (DZ-1b) were, however, not reset, possibly as a result of the larger distance to the fault core and the presence of a calcite vein in between (Fig. 2d). Similarly, the high density of calcite veins in sample DZ-2 (Fig. 4d–f) helped to preserve fault rock domains 1 to 7 during later deformation and/or fluid flow, which localized in the adjacent fault core and, thus, allowed the complete preservation of the Permian deformation features and isotopic signature.

5.2. Strain localization in fault cores

K–Ar geochronology of the incohesive gouge from the fault cores

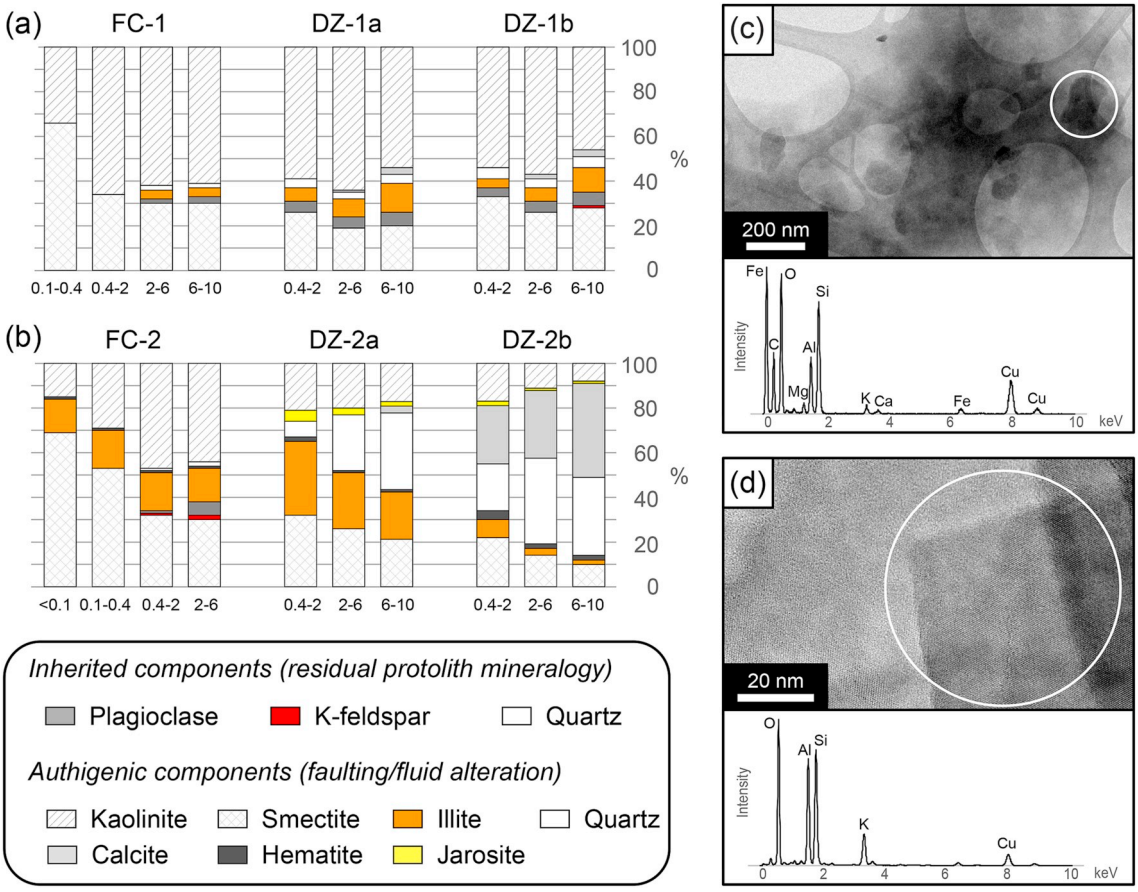

Fig. 8. Mineralogy of the investigated samples. XRD data from (a) Fault I and (b) Fault II. K-bearing minerals are color-coded. Quartz occurs as both protolithic and authigenic. Note that the number of mineral phases generally decreases with smaller grain size. TEM image and corresponding EDS spectrum of the finest grain size fraction of (c) FC-1 and (d) FC-2. (For interpretation of the references to color in this figure legend, the reader is referred to the Web version of this article.)

(FC-1, FC-2) resulted in inclined age spectra, where ages decrease with decreasing grain size (Fig. 9a and b), as reported in many other studies (e.g., Mancktelow et al., 2015; Viola et al., 2016). The age of the coarsest grain size fraction of FC-1 is identical to the ages of the coarsest grain size fractions of DZ-1, and the age of the coarsest grain size fraction of FC-2 is only slightly younger than the Permian age plateau of DZ-2 (Fig. 9a and b). Thus, post-Carboniferous and post-Permian deformation and/or fluid flow did not cause pervasive illite recrystallization of the coarsest dated fractions, but caused significant authigenic and synkinematic growth of grain sizes smaller than 2 µm and 0.4 µm, respectively. The ages of these smaller grain sizes follow different trends down to Jurassic (FC-2) and Cretaceous (FC-1) ages in the finest fractions (Fig. 9a and b). Such inclined age spectra permit various possible interpretations including physical mixing of protolithic and authigenic mineral phases (Torgersen et al., 2015), mixing of various generations of authigenic mineral phases (van der Pluijm et al., 2001), grain-size-dependent Ar loss (Verdel et al., 2012) or a combination of any (Torgersen et al., 2014). Commonly, the age of the finest grain size fraction (< 0.1 µm or less) is assumed to represent the last increment of illite growth (e.g., Viola et al., 2016), generally without knowing the details of the illite-forming process.

The permeability of clay-bearing fault gouges is generally very low (Faulkner, 2004; Faulkner and Rutter, 2003), indicating that the illite from the sampled fault gouge levels (Figs. 2b–4b) actually formed during faulting and not during post-deformational alteration. When dealing with inclined K–Ar age spectra, any grain size fraction, even the finest, has to be generally considered a maximum age of illite authigenesis since a certain amount of contamination by older (both protolithic and authigenic) K-bearing phases cannot be always ruled out (e.g., Davids et al., 2013). In our gouge samples, contamination by protolithic mineral phases is generally minor (Fig. 8a and b, Supplement material 3). Small amounts of K-feldspar were detected in the two coarsest grain size fractions of FC-2, which originates most likely from the granodiorite protolith and would lead to apparently older ages. The effect of thermally activated volume diffusion of radiogenic ^{40}Ar can be disregarded since apatite fission track studies from western Norway indicate paleotemperatures well below c. 200 °C from the early Triassic onwards (Fossen et al., 2017; Ksienzyk et al., 2014). The radiogenic system in these fractions can be considered closed, because closure temperatures of fine-grained illite (effective diffusion radius of 0.1–1.0 µm) were calculated to c. 250–310 °C at cooling rates of 1–10 °C/Ma (Rahl et al., 2011). Mixing of different authigenic mineral generations in the absence of isotopic resetting is thus considered the most likely cause for the obtained inclined K–Ar spectra. Consequently, the intermediate grain sizes (0.1–0.4 µm and 0.4–2 µm for FC-1, 0.1–0.4 µm for FC-2) yield mixed ages, while the age of the finest grain size fractions may be interpreted as maximum age of authigenic illite growth, formed during deformation and possible associated fluid alteration. The ages of the finest fractions are, in any case, the closest to the actual age of the last strain increment recorded by the faults and can therefore be taken as the best approximation of fault reactivation in the Jurassic and Cretaceous, respectively. Indeed, the number of authigenic mineral phases is the lowest in the finest fractions (Fig. 8a and b, Supplement material 3), reducing the effect of mixing mineral phases and generations. Our results support the interpretations done in previous K–Ar illite studies from fault rocks formed within metamorphic terranes showing that the ages of the finest and especially the ones of the coarsest grain size fractions have the greatest potential

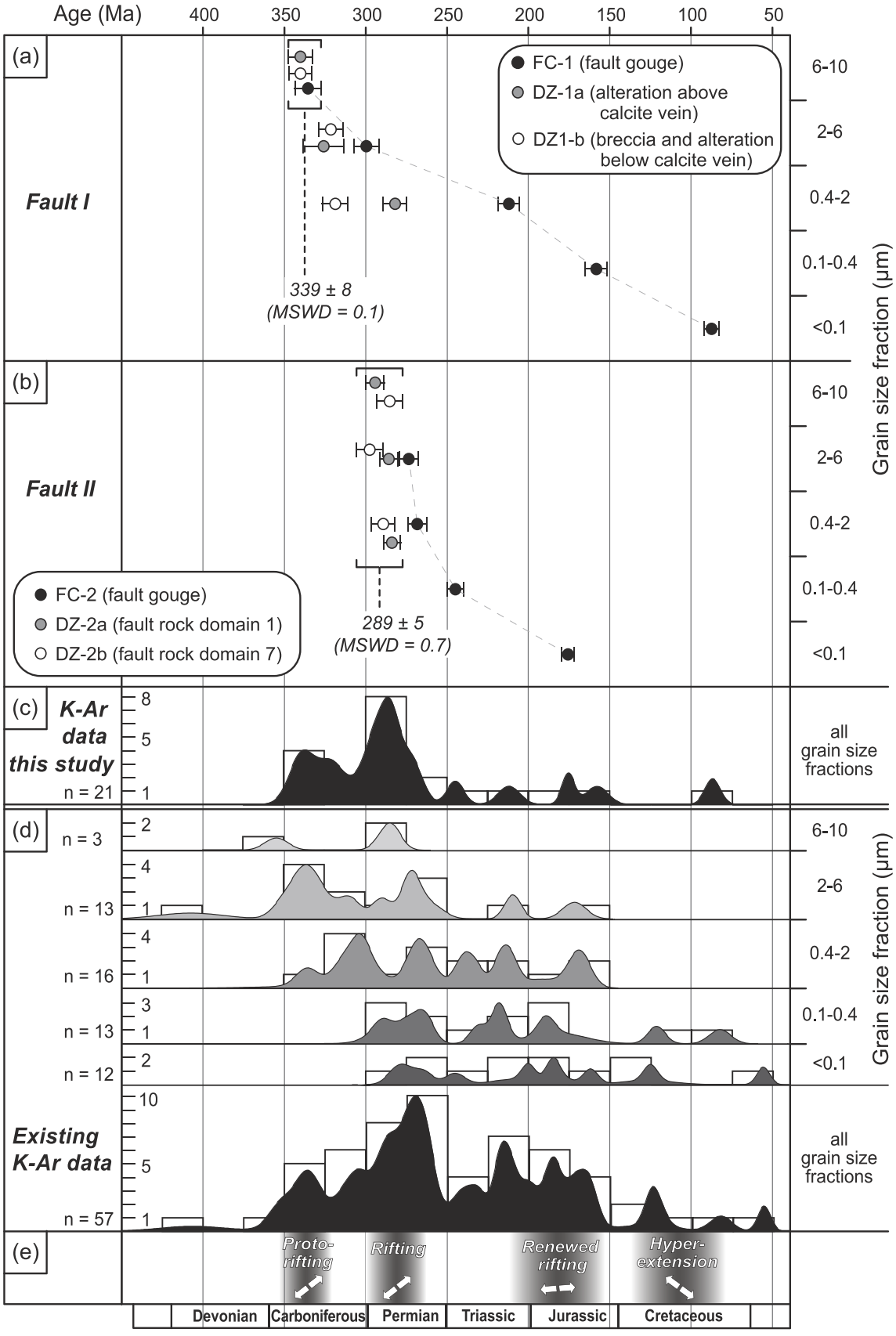

Figure 9. Scheiber et al.

(caption on next page)

Fig. 9. K–Ar data from (a) Fault I and (b) Fault II. Weighted mean ages were calculated for tow age plateaus. (c) Data from both faults compiled as probability density plot and frequency histogram. (d) Compilation of existing clay K–Ar data collected from northern Bømlo (data from Viola et al., 2016 (3 samples, 15 fractions); Fredin et al., 2017 (3 samples, 7 fractions); Scheiber and Viola, 2018 (6 samples, 23 fractions); A. Margreth, unpublished data (3 samples, 12 fractions)). (e) Tectonic interpretation including all K–Ar data from the Bømlo archipelago. Combined probability density plots and frequency histograms were constructed using DensityPlotter (Vermeesch, 2012). Uncertainties of the K–Ar data are reported at the 1σ level and weighted mean ages are quoted at 95% confidence level. n = number.

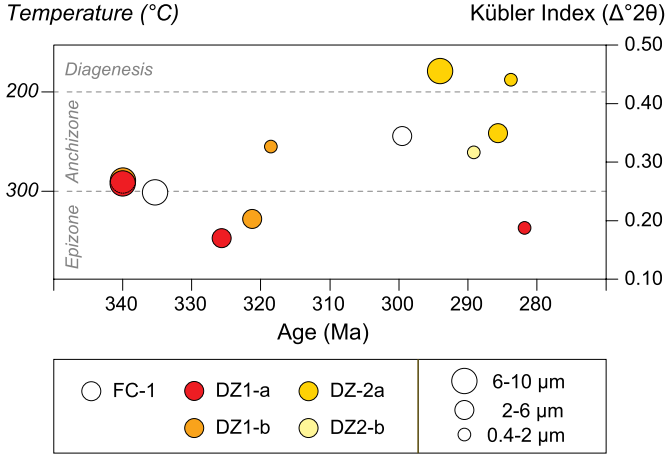

Fig. 10. Illite crystallinity versus age of the dated fractions (cf. Supplement material 3). Kübler indices of 0.25 and 0.42 delimit the anchizone (Kübler and Jaboyedoff, 2000) and correlate to temperatures of c. 300 °C and 200 °C, respectively (e.g., Verdel et al., 2011). Samples from DZ-1 are generally associated with higher temperatures than samples from DZ2. Figure inspired by Ksienzyk et al. (2016).

to date geologically significant events (e.g., Torgersen et al., 2014), which is particularly the case if the ages from different grain size fractions of the same sample are identical and thus define a plateau (Viola et al., 2016).

5.3. Fault zone architecture and model of fault growth evolution

The preserved architecture of a fault zone represents the finite strain state resulting from strain accumulation during the fault zone's entire deformation history (Caine et al., 1996). This architecture may often correspond to across- and along-strike variations of the fault's physical parameters (Fig. 11a). The faults studied here are long-lived fault zones formed within an exhumed metamorphic terrane, which localized multiple episodes of (also seismic) deformation (Scheiber and Viola, 2018; this study). Strain accumulated repeatedly in their fault cores, while the damage zones accommodated only the early increments of their evolution. Sections across these faults reveal changes in the present-day fault zone parameters (Fig. 11a). Thereby, dramatic changes occur across the contact between the fault core and the immediate damage zone. For the current fault zone architecture, strain increases toward the core, while cohesion and permeability decrease. The architectural style of the faults presumably corresponds to a combined conduit-barrier fluid flow system (Caine et al., 1996), where a high amount of clays in the gouge causes low permeability in the fault core while the high fracture density allows for higher permeability in the damage zones (cf. Bense et al., 2013). Accordingly, the amount of protolithic minerals is lower in fault cores than in the damage zone, while the amount of authigenic mineral phases is the highest (Fig. 11a). The bulk content of authigenic phases may be the result of several deformation events (Fig. 11b), each responsible for the growth of a different generation of synkinematic minerals. The amount of authigenic, synkinematic mineral generations translates to the degree of fault reactivation and points to repeated strain localization in the fault cores. In our conceptual sketch (Fig. 11a), K–Ar age plateaus are present in the protolith and in the damage zone adjacent to the fault core whereas the other parts of the fault zone reveal inclined age spectra as a result of mixing protolithic and/or various generation of authigenic minerals. While the anticipated K–Ar age plateau in the protolith could resemble the cooling age of the host rock, the plateau in the damage zone represents authigenesis during fault initiation.

The preservation of the first increment of deformation in the damage zone samples of this study thus indicates that post-fault nucleation deformation localized in the fault cores only and did not affect the mineralogy and isotopic signature of the surrounding damage zone. Consequently, these results permit the discussion of the growth, strength and thickness evolution of the investigated fault zones: Fractures that formed during fault initiation were subsequently flushed by reactive fluids which led to calcite precipitation and associated rock alteration (Figs. 2c–f, 3, 11b). The associated changes in mineralogy led to mechanically heterogeneous behavior during subsequent faulting: the calcite veins were mechanically strong zones, whereas the altered fractures were weak zones, leading to localization of deformation and allowing for slip deformation particularly along the boundaries between preferably oriented calcite veins and altered zones (Figs. 4c–f, 6, 11b). These established continuous slip planes and the associated mechanically weak fault rocks accounted for repeated fault reactivation during later deformation episodes. Slip planes were, however, only partly reactivated and new slip planes may have formed within fault rocks of the fault core, further localizing deformation and narrowing the active part of the fault (Fig. 11b). Fault narrowing may occur due to dynamic weakening caused by the progressive accumulation of clays in the core and due to decreasing deformation temperatures (Rutter et al., 2001).

5.4. Towards a reliable interpretation of a large fault rock K–Ar dataset

The interpretation of clay K–Ar data can be challenging, especially when dealing with large datasets (e.g., Fossen et al., 2016). A comparison of our microstructurally constrained K–Ar data with existing K–Ar data from a c. 50 km^2 area covering the northern Bømlo archipelago (57 dated grain size fractions, 49 of them from within the Rolvsnes granodiorite) contributes to a sound interpretation of the existing K–Ar data and helps to better understand large K–Ar datasets in general. The existing dataset from Bømlo consists of ages obtained from incohesive fault rocks and alteration products not always preserving as clear structural relationships as the samples investigated in the present study. To compare the new K–Ar data with the existing K–Ar dataset, combined diagrams including probability density plots and frequency histograms were produced for all grain size fractions from this study (Fig. 9c), for each of the five grain size fractions of the existing dataset and for all grain size fractions from the existing dataset (Fig. 9d).

Both the Carboniferous and Permian episodes of illite (± jarosite) growth documented in this study are also well-represented as peaks in the probability density plot of all grain size fractions of the existing data (Fig. 9c and d). Interestingly, the Carboniferous ages are not present in the finest grain size fractions, but can only be found in grain sizes > 0.4 µm both in the existing and our new dataset (Fig. 9a and d). Similarly, Permian ages are abundant in the larger grain size fractions and less represented, though present, in the finer grain size fractions. The relationship between large illite grains yielding Carboniferous and Permian ages may be a result of relatively high temperatures (Fig. 10) and, as a consequence, pervasive illite authigenesis during these periods. The Permian age peak from all grain size fractions of the existing K–Ar dataset is slightly younger than the Permian peak of the K–Ar data from this study (Fig. 9c and d). This younger peak in the existing

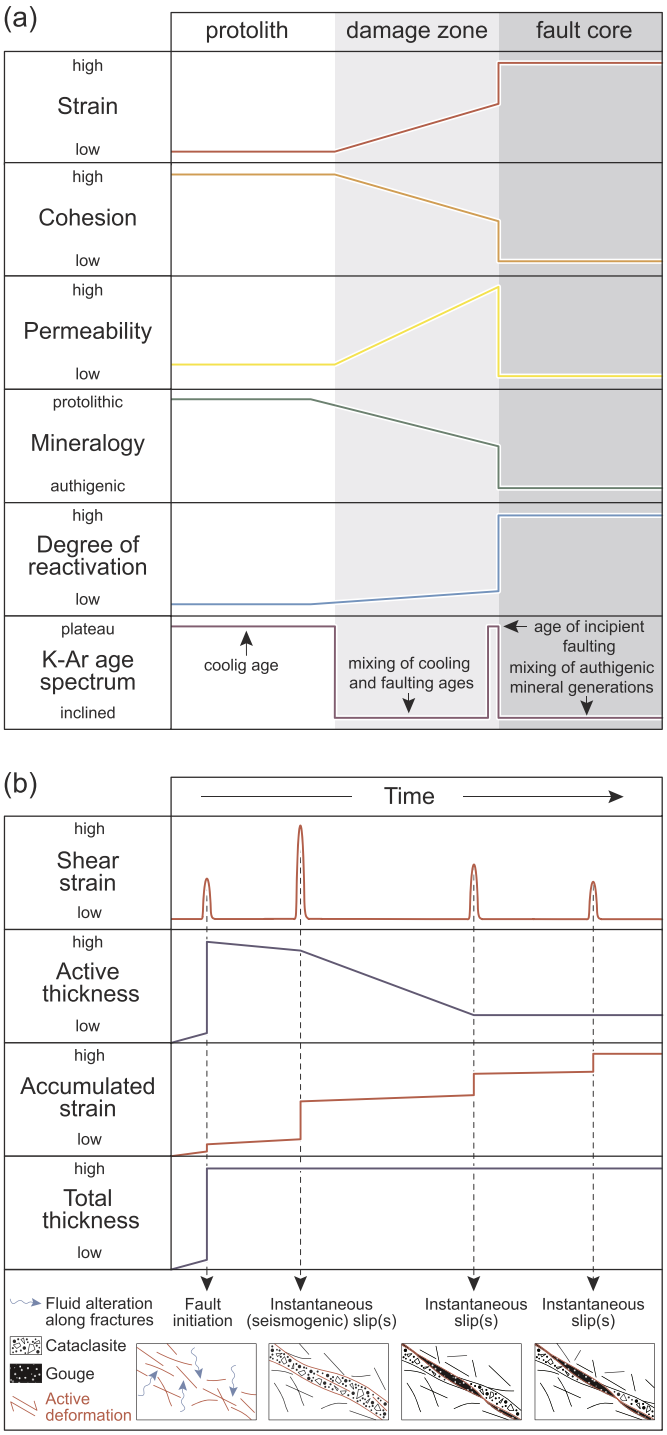

Fig. 11. (a) Conceptual sketch showing the current situation of the investigated faults. Fault zone parameters change from the undeformed host rock to the fault core. Note, however, that these parameters are highly transient during a fault zone's evolution and that this static representation of a fault zone highlights the present-day situation only. (b) Conceptual model of the investigated faults showing the temporal changes in shear strain (active and accumulated) and fault thickness (active and total). Active fractures and faults in cartoon are shown in red. Strain localizes progressively in the fault core, which causes decreasing active thickness. Diagrams based on both quantitative results (mineralogy, K–Ar ages) and qualitative results (strain, cohesion, permeability, degree of reactivation, thickness) of the present study. Figures not to scale. (For interpretation of the references to color in this figure legend, the reader is referred to the Web version of this article.)

dataset correlates with the c. 270 Ma ages of the two coarsest fractions of FC-2 (Fig. 9b) and, in addition, it overlaps in time with the climax of rifting in the Oslo area (Larsen et al., 2008), pointing to protracted and episodic Middle to Late Permian faulting rather than mixing of Late Permian and younger authigenic minerals. However, the preservation of Paleozoic ages in the dataset indicates that these episodes were associated with the most pervasive illite growth up to at least 6–10 µm grain sizes, likely facilitated by relatively high temperatures (c. 300 to 200 °C) as constrained by illite crystallinity (Fig. 10) and supported by published thermochronological data (cf. Ksienzyk et al., 2016 and references therein). Later (Mesozoic) episodes of deformation did not obliterate the Paleozoic isotopic signature.

The ages of the medium grain sizes are generally mixed ages (e.g., Torgersen et al., 2015; this study), derived from physical mixing of protolithic and authigenic mineral phases and/or mixing of various generations of authigenic phases. The ages of the finest grain size fractions are, in turn, generally those being least influenced by mixing with inherited phases of various origins (e.g., Mancktelow et al., 2015; Torgersen et al., 2014; Viola et al., 2016) and can therefore be considered the most suitable to date the last strain increments recorded by faults. In our comparison (Fig. 9c and d), the age of the < 0.1 µm fraction of FC-2 correlates to a Late Triassic-Jurassic cluster of < 0.1 µm ages in the existing dataset, supporting the presence of Jurassic fault reactivation. The distribution of < 150 Ma ages shows three peaks (Fig. 9c and d), an Early Cretaceous (defined by two < 0.1 µm fractions of the existing dataset), a Late Cretaceous (defined by the < 0.1 µm fraction of FC-1) and a Paleogene peak. The Early Cretaceous ages have been interpreted as dating fluid-induced alteration along steeply-dipping c. N–S trending fractures (Scheiber and Viola, 2018; Viola et al., 2016). The Late Cretaceous age probably represents fault reactivation (this study). However, since the Late Cretaceous and the Paleogene peaks are defined by only one < 0.1 µm grain size fraction each, their interpretation has to be taken with care and their geological significance remains poorly constrained.

Considering the complexities and uncertainties involved when interpreting large clay K–Ar datasets, the first order approach based on plotting all the ages obtained within a certain area can provide reliable, i.e. geologically meaningful, results, at least for the most pervasive phases of illite authigenesis (Fossen et al., 2016; this study). A detailed mineralogical investigation of each dated material is, however, necessary when aiming at a grounded interpretation of K–Ar data (cf. Viola et al., 2018).

5.5. Geological implications of the new K–Ar ages

The presented K–Ar data reveal two Paleozoic episodes of crustal extension affecting coastal SW Norway, which can be discussed within the framework of the post-Caledonian evolution of southern Scandinavia and of the North Sea realm. In Scandinavia, the Late Devonian to Early Carboniferous is generally considered as a time period of crustal relaxation after extensive collapse of the Caledonian orogenic belt, with the development of a broad clastic and carbonate shelf in the southern and central North Sea (Ziegler, 1992). However, in SW Norway, major hydrothermal activity along fractures has been dated to c. 371-363 Ma using two-point isochrons of epidote and K-feldspar (Larsen et al., 2003). Additionally, rapid cooling at c. 360-340 Ma identified by diffusion and thermal modeling of K-feldspar has been interpreted as an episode of tectonic unroofing affecting SW Norway (Eide et al., 1999). Two K–Ar illite ages of c. 350 Ma (2–6 and 6–10 µm fractions) obtained from a phyllonite domain of the Goddo fault on Bømlo (Viola et al., 2016) support tectonic activity at this time. Local basins filled with Mid to Late-Carboniferous sediments are preserved in the North Sea and in the Oslo Rift and are interpreted as the result of thermal subsidence due to renewed crustal stretching prior to rift initiation (Larsen et al., 2008). Therefore, the Carboniferous, 339 ± 8 Ma deformation-induced fluid-related alteration phase

identified in this study (Fig. 9a) may correspond to a specific tectonic event of incipient crustal extension (Fig. 9e).

In the Late Carboniferous and Early Permian extensive magmatic provinces developed within northern Europe, with the Oslo Rift being one of the major features onshore (Larsen et al., 2008; Neumann et al., 2004; Torsvik et al., 2008). Peak magmatic activity occurred at about 300-280 Ma (op. cit.), an age range which predates pulses of doleritic dyke intrusion along coastal SW Norway in the Permo-Triassic (Fossen and Dunlap, 1999; Torsvik et al., 1997). Our new faulting age of 289 ± 5 Ma (Fig. 9b) coincides with this peak magmatism and can be thus considered as a distinct phase of NE-SW extension during rifting (Fig. 9e). This deformation was accommodated by occasionally seismogenic top-to-the-NE slip along NNW-SSE striking faults, as indicated by the presence of pseudotachylyte (Fig. 5c–f). This fault orientation is compatible with major structural elements in the central North Sea (e.g., Ziegler, 1992), which is interpreted to originate from Permo-Carboniferous extension (Heeremans and Faleide, 2004). Permo-Carboniferous structures were reactivated during later episodes of deformation (e.g., Scheiber and Viola, 2018; Viola et al., 2016). However, E-W to NW-SE extension directions are constrained for Mesozoic episodes of crustal extension (Fig. 9e), which is in accordance with the dominating c. N–S strike of Mesozoic structural elements, such as for example the Viking Graben or the Stord Basin (Fig. 1b), and the general NE-SW trend of the Norwegian Sea (Fig. 1a).

6. Conclusions

Our outcrop- to micro-scale study from two fault zones in an Ordovician granodiorite in SW Norway shows that samples from cohesive damage zones offer the potential to preserve structural, mineralogical and isotopic characteristics from the earliest increments of a fault zone's evolution, even if the fault core was repeatedly active throughout the fault's later history. Strain during fault reactivation is confined to the fault core due to strain localization leading to fault narrowing. The fault core is, at present, characterized by incohesive fault rocks, large amount of secondary clay mineral assemblages, and large age spreads in K–Ar age-versus-grain-size spectra. Therefore, it is generally a difficult task to constrain the timing of fault initiation and to decipher the complex reactivation history of long-lived brittle fault cores. Microstructurally-constrained K–Ar geochronology applied to the damage zone samples, however, resulted in narrow K–Ar age ranges and even age plateaus, which can be interpreted as recording fault initiation. These ages invariably constrain proto-(North Sea)-rift veining and associated fluid alteration in the Carboniferous (339 ± 8 Ma) and Early Permian rifting (289 ± 5 Ma) accommodated by pseudotachylyte-bearing top-to-the-NE normal faults. The ages of the coarsest grain sizes of fault gouge from the corresponding adjacent fault cores yield similar ages, indicating that the Paleozoic deformation episodes were the most pervasive and associated with higher temperatures, and that subsequent Mesozoic fault reactivation and/or fluid flow caused authigenic mineral growth up to only small grain sizes within the fault core. This age distribution matches the high density of Carboniferous and Permian clay K–Ar ages in the existing dataset from the area.

Acknowledgements

This study was performed in the course of the BASE project ("Basement fracturing and weathering on- and offshore Norway - Genesis, age, and landscape development"), a joint research project hosted by the Geological Survey of Norway (NGU) and funded by Det Norske Oljeselskap (now Aker BP ASA), Lundin Petroleum, Maersk Oil, Wintershall and the NGU. Clea Fabian and Ruikai Xie from the NGU laboratory and Andrew Todd and Mark Raven from CSIRO are thanked for assistance with sample preparation, K–Ar analysis, and XRD analysis, respectively. TEM analysis was performed at the NORTEM infrastructure at the TEM Gemini Centre of the Norwegian University of Science and Technology (NTNU). Reviews by Sam Haines and one anonymous reviewer are greatly appreciated and Cees Passchier is thanked for the editorial handling of the manuscript.

Appendix A. Supplementary data

Supplementary data to this article can be found online at https://doi.org/10.1016/j.jsg.2019.103868.

References

Altaner, S.P., Ylagan, R.F., 1997. Comparison of structural models of mixed-layer illite/smectite and reaction mechanisms of smectite illitization. Clay Clay Miner. 45, 517–533.
Andersen, T.B., Jansen, Ø.J., 1987. The Sunnhordland Batholith, W. Norway: regional setting and internal structure, with emphasis on the granitoid plutons. Norw. J. Geol. 67, 159–183.
Bense, V.F., Gleeson, T., Loveless, S.E., Bour, O., Scibek, J., 2013. Fault zone hydrogeology. Earth Sci. Rev. 127, 171–192.
Caine, J.S., Evans, J.P., Forster, C.B., 1996. Fault zone architecture and permeability structure. Geology 24, 1025–1028.
Clauer, N., 2013. The K-Ar and 40Ar/39Ar methods revisited for dating fine-grained K-bearing clay minerals. Chem. Geol. 354, 163–185.
Corfu, F., Andersen, T.B., Gasser, D., 2014. The Scandinavian Caledonides: main features, conceptual advances and critical questions. Geol. Soc. Lond. Spec. Publ. 390, 9–43.
Cowan, D.S., 1999. Do faults preserve a record of seismic slip? A field geologist's opinion. J. Struct. Geol. 21, 995–1001.
Davids, C., Wemmer, K., Zwingmann, H., Kohlmann, F., Jacobs, J., Bergh, S.G., 2013. K–Ar illite and apatite fission track constraints on brittle faulting and the evolution of the northern Norwegian passive margin. Tectonophysics 608, 196–211.
Eide, E.A., Torsvik, T.H., Andersen, T.B., Arnaud, N.O., 1999. Early carboniferous unroofing in western Norway: a tale of alkali feldspar thermochronology. J. Geol. 107, 353–374.
Faulkner, D.R., 2004. A model for the variation in permeability of clay-bearing fault gouge with depth in the brittle crust. Geophys. Res. Lett. 31.
Faulkner, D.R., Rutter, E.H., 2003. The effect of temperature, the nature of the pore fluid, and subyield differential stress on the permeability of phyllosilicate-rich fault gouge. J. Geophys. Res.: Solid Earth 108.
Fossen, H., 2010. Extensional tectonics in the north atlantic caledonides: a regional view. Geol. Soc. Lond. Spec. Publ. 335, 767–793.
Fossen, H., Dunlap, W.J., 1999. On the age and tectonic significance of Permo-Triassic dikes in the Bergen-Sunnhordland region, southwestern Norway. Norw. J. Geol. 79, 169–178.
Fossen, H., Khani, H.F., Faleide, J.I., Ksienzyk, A.K., Dunlap, W.J., 2016. Post-caledonian Extension in the West Norway–northern North Sea Region: the Role of Structural Inheritance. Geological Society, London Special Publications 439.
Fossen, H., Ksienzyk, A.K., Jacobs, J., 2017. Correspondence: challenges with dating weathering products to unravel ancient landscapes. Nat. Commun. 8, 1502.
Fredin, O., Viola, G., Zwingmann, H., Sørlie, R., Brönner, M., Lie, J.-E., Grandal, E.M., Müller, A., Margreth, A., Vogt, C., Knies, J., 2017. The inheritance of a Mesozoic landscape in western Scandinavia. Nat. Commun. 8, 14879.
Haines, S.H., van der Pluijm, B.A., 2012. Patterns of mineral transformations in clay gouge, with examples from low-angle normal fault rocks in the western USA. J. Struct. Geol. 43, 2–32.
Heeremans, M., Faleide, J.I., 2004. Late carboniferous-permian tectonics and magmatic activity in the skagerrak, kattegat and the north Sea. Geol. Soc. Lond. Spec. Publ. 223, 157–176.
Kirkpatrick, J.D., Rowe, C.D., 2013. Disappearing ink: how pseudotachylytes are lost from the rock record. J. Struct. Geol. 52, 183–198.
Koehl, J.-B.P., Bergh, S.G., Wemmer, K., 2018. Neoproterozoic and post-Caledonian exhumation and shallow faulting in NW Finnmark from K–Ar dating and p/ T analysis of fault rocks. Solid Earth 9, 923–951.
Ksienzyk, A.K., Dunkl, I., Jacobs, J., Fossen, H., Kohlmann, F., 2014. From orogen to passive margin: constraints from fission track and (U–Th)/He analyses on Mesozoic uplift and fault reactivation in SW Norway. Geol. Soc. Lond. Spec. Publ. 390, 679–702.
Ksienzyk, A.K., Wemmer, K., Jacobs, J., Fossen, H., Schomberg, A.C., Süssenberger, A., Lünsdorf, N.K., Bastesen, E., 2016. Post-Caledonian brittle deformation in the Bergen area, West Norway: results from K–Ar illite fault gouge dating. Norw. J. Geol. 96, 275–299.
Kübler, B., Jaboyedoff, M., 2000. Illite crystallinity. Comptes Rendus Acad. Sci. - Ser. IIA Earth Planet. Sci. 331, 75–89.
Lanson, B., Beaufort, D., Berger, G., Bauer, A., Cassagnabère, A., Meunier, A., 2002. Authigenic kaolin and illitic minerals during burial diagenesis of sandstones: a review. Clay Miner. 37, 1–22.
Larsen, B.T., Olaussen, S., Sundvoll, B., Heeremans, M., 2008. The Permo-Carboniferous Oslo Rift through six stages and 65 million years. Episodes 31, 52–58.
Larsen, Ø., Fossen, H., Langeland, K., Pedersen, R.-B., 2003. Kinematics and timing of polyphase post-Caledonian deformation in the Bergen area, SW Norway. Norw. J. Geol. 83, 149–165.
Lin, A., 2008. Fossil Earthquakes: the Formation and Preservation of Pseudotachylytes. Springer, Berlin Heidelberg New York.

Mancktelow, N., Zwingmann, H., Campani, M., Fügenschuh, B., Mulch, A., 2015. Timing and conditions of brittle faulting on the silltal-brenner fault zone, eastern alps (Austria). Swiss J. Geosci. 108, 305–326.
Marchesini, B., Garofalo, P.S., Menegon, L., Mattila, J., Viola, G., 2019. Fluid-mediated, brittle–ductile deformation at seismogenic depth – Part 1: fluid record and deformation history of fault veins in a nuclear waste repository (Olkiluoto Island, Finland). Solid Earth 10, 809–838.
Neumann, E.-R., Wilson, M., Heeremans, M., Spencer, E.A., Obst, K., Timmerman, M.J., Kirstein, L., 2004. Carboniferous-Permian rifting and magmatism in southern Scandinavia, the North Sea and northern Germany: a review. Geol. Soc. Lond. Spec. Publ. 223, 11–40.
Pevear, D.R., 1999. Illite and hydrocarbon exploration. Proc. Natl. Acad. Sci. 96, 3440–3446.
Rahl, J.M., Haines, S.H., van der Pluijm, B.A., 2011. Links between orogenic wedge deformation and erosional exhumation: evidence from illite age analysis of fault rock and detrital thermochronology of syn-tectonic conglomerates in the Spanish Pyrenees. Earth Planet. Sci. Lett. 307, 180–190.
Rutter, E.H., Holdsworth, R.E., Knipe, R.J., 2001. The Nature and Tectonic Significance of Fault-Zone Weakening: an Introduction, vol.186. Geological Society, London, Special Publications, pp. 1–11.
Scheiber, T., Viola, G., 2018. Complex bedrock fracture patterns: a multipronged approach to resolve their evolution in space and time. Tectonics 37, 1030–1062.
Scheiber, T., Viola, G., Wilkinson, C.M., Ganerød, M., Skår, Ø., Gasser, D., 2016. Direct 40Ar/39Ar dating of late ordovician and silurian brittle faulting in the southwestern Norwegian caledonides. Terra. Nova 28, 374-382.
Schneider, C.A., Rasband, W.S., Eliceiri, K.W., 2012. NIH Image to ImageJ: 25 years of image analysis. Nat. Methods 9, 671.
Sibson, R.H., 1977. Fault rocks and fault mechanisms. J. Geol. Soc. 133, 191–213.
Snoke, A.W., Tullis, J., Todd, V.R., 2014. Fault-related Rocks: a Photographic Atlas. Princeton University Press.
Solum, J.G., van der Pluijm, B.A., Peacor, D.R., 2005. Neocrystallization, fabrics and age of clay minerals from an exposure of the Moab Fault, Utah. J. Struct. Geol. 27, 1563–1576.
Stephens, M.B., Gee, D.G., 1989. Terranes and polyphase accretionary history in the Scandinavian Caledonides. GSA (Geol. Soc. Am.) Spec. Pap. (Reg. Stud.) 230, 17–30.
Tagami, T., 2012. Thermochronological investigation of fault zones. Tectonophysics 538, 67–85.
Torgersen, E., Viola, G., Zwingmann, H., Harris, C., 2014. Structural and temporal evolution of a reactivated brittle–ductile fault – Part II: timing of fault initiation and reactivation by K–Ar dating of synkinematic illite/muscovite. Earth Planet. Sci. Lett. 407, 221–233.
Torgersen, E., Viola, G., Zwingmann, H., Henderson, I.H.C., 2015. Inclined K–Ar illite age spectra in brittle fault gouges: effects of fault reactivation and wall-rock contamination. Terra. Nova 27, 106–113.
Torsvik, T.H., Andersen, T.B., Eide, E.A., Walderhaug, H.J., 1997. The age and tectonic significance of dolerite dykes in western Norway. J. Geol. Soc. 154, 961–973.
Torsvik, T.H., Smethurst, M.A., Burke, K., Steinberger, B., 2008. Long term stability in deep mantle structure: evidence from the ~ 300 Ma skagerrak-centered large igneous province (the SCLIP). Earth Planet. Sci. Lett. 267, 444–452.
van der Pluijm, B.A., Hall, C.M., Vrolijk, P.J., Pevear, D.R., Covey, M.C., 2001. The dating of shallow faults in the Earth's crust. Nature 412, 172–175.
Verdel, C., Niemi, N., Pluijm, B.A.v.d., 2011. Variations in the illite to muscovite transition related to metamorphic conditions and detrital muscovite content: insight from the paleozoic passive margin of the southwestern United States. J. Geol. 119, 419–437.
Verdel, C., van der Pluijm, B.A., Niemi, N., 2012. Variation of illite/muscovite 40Ar/39Ar age spectra during progressive low-grade metamorphism: an example from the US Cordillera. Contrib. Mineral. Petrol. 164, 521–536.
Vermeesch, P., 2012. On the visualisation of detrital age distributions. Chem. Geol. 312–313, 190–194.
Viola, G., Scheiber, T., Fredin, O., Zwingmann, H., Margreth, A., Knies, J., 2016. Deconvoluting complex structural histories archived in brittle fault zones. Nat. Commun. 7, 13448.
Viola, G., Torgersen, E., Mazzarini, F., Musumeci, G., Lelij, R., Schönenberger, J., Garofalo, P.S., 2018. New constraints on the evolution of the inner northern apennines by K-Ar dating of late miocene-early pliocene compression on the island of elba. Italy. Tectonics 37, 3229–3243.
Viola, G., Zwingmann, H., Mattila, J., Käpyaho, A., 2013. K-Ar illite age constraints on the Proterozoic formation and reactivation history of a brittle fault in Fennoscandia. Terra. Nova 25, 236–244.
Vrolijk, P., van der Pluijm, B.A., 1999. Clay gouge. J. Struct. Geol. 21, 1039–1048.
Warr, L.N., 2018. A new collection of clay mineral 'Crystallinity' Index Standards and revised guidelines for the calibration of Kübler and Árkai indices. Clay Miner. 53, 339–350.
Ylagan, R.F., Kim, C.S., Pevear, D.R., Vrolijk, P.J., 2002. Illite polytype quantification for accurate K-Ar age determination. Am. Mineral. 87, 1536–1545.
Ziegler, P.A., 1992. North Sea rift system. Tectonophysics 208, 55–75.
Zwingmann, H., Mancktelow, N., 2004. Timing of Alpine fault gouges. Earth Planet. Sci. Lett. 223, 415–425.
Zwingmann, H., Mancktelow, N., Antognini, M., Lucchini, R., 2010. Dating of shallow faults: new constraints from the AlpTransit tunnel site (Switzerland). Geology 38, 487–490.